



# Multiscale and multimodel simulation of Bloch-point dynamics

Christian Andreas,<sup>1,2,\*</sup> Attila Kákay,<sup>1</sup> and Riccardo Hertel<sup>2</sup>

<sup>1</sup>*Peter Grünberg Institut (PGI-6), Forschungszentrum Jülich GmbH, D-52428 Jülich, Germany*

<sup>2</sup>*Institut de Physique et Chimie des Matériaux de Strasbourg, Université de Strasbourg, CNRS UMR 7504, Strasbourg, France*

(Received 4 December 2013; revised manuscript received 5 February 2014; published 3 April 2014)

We present simulation results on the structure and dynamics of micromagnetic point singularities with atomistic resolution. This is achieved by embedding an atomistic computational region into a standard micromagnetic algorithm. Several length scales are bridged by means of an adaptive mesh refinement and a seamless coupling between the continuum theory and a Heisenberg formulation for the atomistic region. The code operates on graphical processing units and is able to detect and track the position of strongly inhomogeneous magnetic regions. This enables us to reliably simulate the dynamics of Bloch points, which means that a fundamental class of micromagnetic switching processes can be analyzed with unprecedented accuracy. We test the code by comparing it with established results and present its functionality with the example of a simulated field-driven Bloch-point motion in a soft-magnetic cylinder.

DOI: [10.1103/PhysRevB.89.134403](https://doi.org/10.1103/PhysRevB.89.134403)

PACS number(s): 75.78.Cd, 75.70.Kw, 75.60.Jk, 02.40.Xx

## I. INTRODUCTION

Textbooks on ferromagnetism typically list three fundamental modes for magnetization reversal: buckling, curling, and rotation in unison [1–3]. Those basic instabilities were derived analytically for homogeneously magnetized ferromagnetic cylinders in an external magnetic field [4]. Over the past two decades, high-resolution imaging techniques and advanced micromagnetic simulation studies have shown that the magnetization reversal is usually a much more complex process than predicted by analytic theory. It may involve the nucleation and the propagation of vortices, antivortices, as well as domain walls of various types, and it is usually accompanied by a broad spectrum of spin-wave excitations. Such complications arise mainly from finite-size effects. The three fundamental reversal modes are only correct for the hypothetical case of an infinitely extended ferromagnetic cylinder; but the end of a real cylinder acts as a nucleation site, leading to a completely different type of reversal. The importance of the end of a cylinder was investigated by Arrott and co-workers [5,6]. They predicted that point singularities play a decisive role in the switching of soft-magnetic cylinders. Such point singularities of the magnetization are known as Bloch points. They were described by Feldtkeller [7] and later by Döring [8] and they represent a fundamental class of micromagnetic structures.

## II. TOPOLOGICAL DEFECTS AND SINGULARITIES

The simulation of Bloch points is connected with great difficulties. A reason for this is that they represent singularities in the continuum theory of micromagnetism. As a prototype and as the simplest version of a large family of Bloch-point structures, one can imagine such singularities as a centrosymmetric hedgehog-type arrangement, where the magnetization vectors are radially oriented away from the Bloch point. For symmetry reasons, no magnetization direction can be assigned to the point at the center of such a structure.

This violates a fundamental aspect of micromagnetic theory, which treats the magnetization as a continuous and smooth vector field with constant magnitude at every point within the ferromagnet. Bloch points are hence topological defects in the vector field of the magnetization. Around these points, the magnetization is maximally inhomogeneous, which causes the exchange energy density to diverge. In spite of this singularity in the energy density, the total energy of a Bloch-point structure remains finite. The strong inhomogeneity generates another, from a practical viewpoint, even more important difficulty: The exchange energy density formulation in micromagnetism relies on the assumption of a smooth variation of the magnetization on the length scale of the atomic lattice constant. Based on this assumption, which is perfectly valid in the case of ordinary micromagnetic structures such as vortices or domain walls, it is easy to derive that the exchange field is proportional to the Laplacian of the magnetization, which is used, e.g., in any micromagnetic code based on the Landau-Lifshitz-Gilbert equation [9–11]. Removing the approximation of a slow spatial variation makes the entire calculation of the exchange field questionable. In addition to the difficulties concerning the theoretical foundations, the simulation of singularities in continuum theories is a delicate subject. The discretization error displays a power-law behavior as a function of the cell size [12], with a low convergence rate that makes it particularly difficult to obtain reliable solutions. The most careful studies on Bloch points, therefore, make use of various grids and extrapolate the computed values to infinite discretization density [13,14]. This procedure is tedious, but it can at least remove the numerical artifacts.

## III. THE MULTISCALE PROBLEM

It appears that all difficulties connected with Bloch points stem from micromagnetic theory, as it is also the case, e.g., for the correct treatment of nanoparticle grain boundaries [15]. If an atomistic Heisenberg model [16] is used, nothing prevents neighboring atomistic magnetic moments from being strongly misaligned. Moreover, once the assumption of a continuous vector field of the magnetization is replaced by a discrete set of magnetic moments and the ferromagnetic

\*Corresponding author: christian.andreas@ipcms.unistra.fr

exchange is treated with a Heisenberg term instead of the micromagnetic formulation, the singularities disappear and the problems dissolve. However, such an approach implies an atomistic treatment of the entire ferromagnet—a model that is extremely expensive from a computation point of view and which constitutes a dramatic waste of resources since almost the entire ferromagnet could safely be simulated at significantly lower computational costs within the framework of micromagnetism. One might thus be tempted to discard the regions outside the Bloch point and investigate only the volume containing the Bloch point. However, as pointed out in the textbook of Hubert and Schäfer [17] (p. 252), “a singularity has always to be analyzed together with the environment into which it is embedded.” To better understand this, an analogy with basic astronomy might help. In stars, the weak but long-range gravitational force provides the confinement of a plasma with sufficiently high energy density to overcome the Coulomb barrier in nuclear fusion processes. Similarly, the relatively weak but cumulative long-range magnetostatic interaction can stabilize a highly energetic Bloch point in the volume of a sufficiently large ferromagnet. The Bloch-point structure would immediately dissolve if it was removed from the mesoscopic environment into which it is embedded. The situation is, therefore, extremely complicated to treat numerically, since different length scales and energy densities have to be combined. A recent approach to treat Bloch points consists of dropping the micromagnetic assumption of constant magnitude of the magnetization and allowing for its gradual reduction to zero in the vicinity of the Bloch point by means of the Landau-Lifshitz-Bloch equation [18]. Other authors have suggested a phenomenological Landau-type energy term to account for the reduction of the magnetization in Bloch points [19]. This has provided the basis for a remarkable numerical study on its static three-dimensional configuration [20]. These approaches solve the topological part of the problem because they remove the character of a point defect from these structures. But as far as the exchange representation is concerned, the difficulties remain, and only a combination of an atomistic Heisenberg model with a continuum model seems to be able to overcome this obstacle. Important previous work on multiscale simulations in micromagnetics has been reported by Jourdan *et al.* [21]. Their method was based on an adaptively refined finite-difference grid with the smallest cell size equivalent to the atomic lattice constant. The atomistic region was carefully connected to the micromagnetic part with a suitable coarse-graining transition. The application of this method is, however, restricted to the case of a simple cubic lattice, which usually does not correspond to the crystalline structure of ferromagnets. Other approaches [15,22] consisted of coupling a specific atomistic region to the micromagnetic continuum. The main difference between our model and those reported before is that the atomistic region of interest is mobile and capable of tracking strong inhomogeneities wherever they occur.

In order to obtain the largest possible flexibility concerning the lattice type and the sample geometry, while being able to atomistically resolve the position of the Bloch-point singularity, we have developed a different type of multiscale-multimodel algorithm, which is described in detail in this paper. A multiscale model extends our graphics processing

unit (GPU) accelerated micromagnetic code TETRAMAG [23], which solves the Landau-Lifshitz-Gilbert [9–11] equation using a finite-element/boundary-element method (FEM/BEM). We implemented an atomistic Heisenberg model with realistic crystalline structure to treat the exchange interaction in quasiclassical approximation. The dynamics of the magnetic moments in the atomistic region is coupled to the motion of the magnetization into which the structure is embedded. In order to investigate the motion of the Bloch point, the atomistic part moves within the ferromagnet in a self-adaptive way, by recognizing the position of the Bloch point.

After a short description of the fundamental equations, we discuss the implementation of the multiscale/multimodel algorithm. In Sec. VI, we demonstrate the functionality of the program on the basis of the well-defined system of a gyrating vortex, which is a complicated yet nonsingular structure. This is to ascertain that the multiscale/multimodel simulation does not alter the results obtained from established micromagnetic theory. In the last part, we present an example where we employ the code to simulate the field-driven motion of a Bloch point in a soft-magnetic cylinder with atomistic resolution in the core region.

#### IV. BASIC EQUATIONS

For the multiscale/multimodel simulation, we assume ferromagnetic crystalline samples and combine the representation of exchange energy in the micromagnetic (MM) model with the one of the Heisenberg (Hei) formulation. In micromagnetic theory, the exchange energy density is defined as [2]

$$e_{xc} = A \sum_{\alpha}^{x,y,z} \left( \frac{\partial \mathbf{m}}{\partial x_{\alpha}} \right)^2, \quad (1)$$

where  $A$  is the exchange stiffness and  $\mathbf{m}$  is the normalized magnetization vector. The classical Heisenberg model [16] represents the exchange energy density at a lattice site  $i$  according to

$$e_{xc}^{(i)} = - \sum_j \frac{J_{ij}}{V_i} \mathbf{s}_i \cdot \mathbf{s}_j = - \sum_j \frac{J_{ij}}{V_i} \cos \theta_{ij}, \quad (2)$$

where  $V_i$  is the volume ascribed to the lattice site  $i$ , and  $J_{ij}$  is the exchange constant between the magnetic moments  $i$  and  $j$  with orientation  $\mathbf{s}_i$  and  $\mathbf{s}_j$  enclosing the angle  $\theta_{ij}$ .

Equation (2) can be expanded into a Taylor series,

$$e_{xc}^{(i)} = -e_0 + \sum_j J_{ij}/V_i \left[ \frac{\theta_{ij}^2}{2} - \mathcal{O}(\theta_{ij}^4) \right], \quad (3)$$

with a constant offset energy density  $e_0$  that can be omitted. To derive the exchange stiffness  $A_i$  for a given set of exchange constants  $J_{ij}$  in the vicinity of the lattice site  $i$ , a spin spiral with arbitrary wavelength  $\lambda \gg a$  can be used as a reference structure ( $a$  is the lattice constant). Owing to the isotropy of Eqs. (1) and (2), the direction of the spin spiral can be chosen without loss of generality along the  $x$  axis,

$$\mathbf{m}(x) = \begin{pmatrix} \sin(\pi x/\lambda) \\ \cos(\pi x/\lambda) \\ 0 \end{pmatrix}. \quad (4)$$

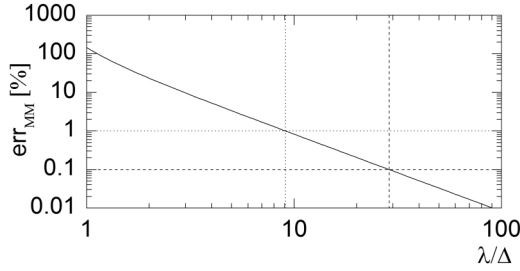


FIG. 1. Error estimate for the intrinsic deviation of the micromagnetic exchange energy formulation from a Heisenberg calculation. The error is displayed for the test case of a spin spiral of wavelength  $\lambda$ , where  $\Delta$  is the distance between neighboring magnetic moments along the direction of the spin spiral.

The values can then be calibrated such that the micromagnetic and Heisenberg exchange are identical. By considering only the first nonvanishing part of the Taylor series, a comparison between Eqs. (1) and (3) yields the following condition for the spin spiral:

$$\sum_j \frac{J_{ij}}{2V_i} \left( \pi \frac{\Delta x_{ij}}{\lambda} \right)^2 = A_i \frac{\pi^2}{\lambda^2}, \quad (5)$$

where  $\Delta x_{ij}$  represents the distance between the lattice sites  $i$  and  $j$  along  $x$ . Discarding the obviously irrelevant case  $\lambda = 0$  yields a direct connection between the micromagnetic exchange constant  $A_i$  and the Heisenberg exchange tensor  $J_{ij}$ . Since the micromagnetic model acts in volumes much larger than the volume  $V_i$  associated to a single atom, a straightforward way to determine the micromagnetic exchange stiffness  $A$  is to compute a volume-weighted average of the values  $A_i$ ,

$$A = \frac{1}{\sum_i V_i} \sum_{i,j} J_{ij} \Delta x_{ij}^2 / 2. \quad (6)$$

In a single-phase monocrystalline material, such an averaging is not necessary, but it can be important in more complex materials. For monoatomic lattices, the above equation allows one to estimate the difference between the micromagnetic and the Heisenberg model in the case of short wavelengths  $\lambda$ . On a distance  $\Delta$  along the spin spiral with wavelength  $\lambda$ , the error of the micromagnetic term introduced by truncating the Taylor series (3) is

$$\text{err}_{\text{MM}}(\Delta, \lambda) = \frac{\pi^2 \Delta^2}{2\lambda^2} \left[ 1 - \cos \left( \frac{\pi \Delta}{\lambda} \right) \right]^{-1} - 1. \quad (7)$$

Figure 1 displays the systematic error which, according to Eq. (7), results from the small-angle approximation in the micromagnetic formulation of the exchange energy density. This equation was derived assuming a Heisenberg model with nearest-neighbor interaction. The dotted and the dashed line indicate the minimum spin-wave half length below which the micromagnetic error exceeds 0.1% ( $\lambda < 29\Delta$ ) and 1% ( $\lambda < 9\Delta$ ), respectively.

## V. IMPLEMENTATION

Implementations of atomistic/continuum multiscale models in other domains of physics [24] are based on the refinement

of the discretization grid used in the continuum model, such that the cell size is of the order of atomic distances in the region of interest. Finally, an atomistic treatment is implanted on the discretization points of the grid to combine the equations governing the atomistic effect with those describing the continuum. As long as the region of interest remains at the same position, the interaction matrices can be preprocessed, meaning that the simulation can be performed efficiently. In the cases that we wish to study, however, the region of interest (i.e., the Bloch point) propagates through the sample. In this case, the standard procedure would require a dynamic remeshing, resulting in prohibitively high numerical costs. We, therefore, chose another approach, which consists of leaving the sample mesh unchanged and tracing the region of interest with a spherical structure implanted into the sample. This *multiscale sphere* (MS) can be preprocessed and incorporates the Heisenberg model as well as the mesh that coarsens with increasing distance from the center of the MS. The MS used in the simulation is shown in Fig. 2, where a part has been removed to display the internal structure. The Heisenberg region in its center (blue part in Fig. 2) represents the atomic lattice, which is surrounded by a finite-element mesh (green and orange regions in Fig. 2) with a shell in which a gradual transition between the atomistic and the sample discretization length scale is achieved. An interface region (blue to green shading in Fig. 2) accounts for this transition from the micromagnetic to the Heisenberg model, while the outer part is treated entirely in the framework of micromagnetism. Only the orange region inherits its magnetic properties directly from the surrounding finite-element structure. The details of the coupling will be described in Sec. V C.

### A. Multiscale sphere construction

In the core region of the sphere, a ferromagnetic crystalline structure is modeled by placing magnetic moments at the

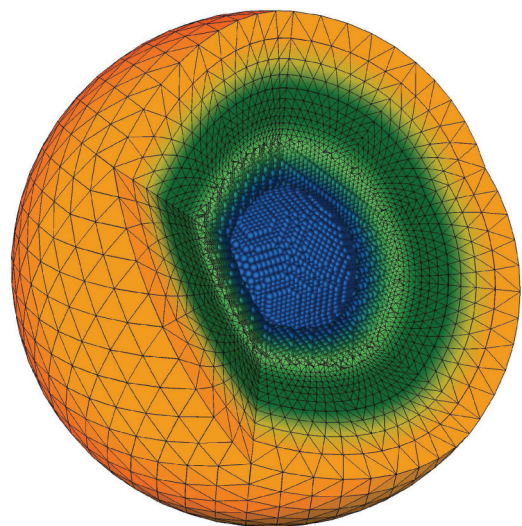


FIG. 2. (Color) Two different models are used to calculate the exchange interaction in the MS: Heisenberg (blue) and micromagnetic (green and orange). The green to orange shading illustrates a transition region from the outer sample to the MS, inside of which the MS stamps its properties onto the sample (green), and vice versa (orange).

atomistic positions of the Bravais lattice. This is performed within a sphere of radius  $R_1$ . The atomistic positions also serve as the vertices for tetrahedral meshing in the inner part of the sphere. We thereby obtain a structure where the positions of atomic magnetic moments and vertices of finite-element cells coincide.

The core of the MS consists of three parts which are arranged according to the following conventions:

(i) In the inner core, a pure Heisenberg model is employed for radii smaller than  $R_H$ . The location of the sphere is determined from the error estimate according to Eq. (7). We assume that a local error between 0.1% to 1% is acceptable; if this threshold is trespassed, the MS is either displaced accordingly, or a new MS is generated.

(ii) Within a transition region of thickness  $\delta_T$ , the exchange energy is calculated by a weighted average of the result from both the Heisenberg model and the continuum representation. If  $r$  is the distance from the center of the MS, we use

$$E_{\text{multiscale}} = f(r)E_{\text{Hei}} + [1 - f(r)]E_{\text{MM}}, \quad (8)$$

where  $f(r)$  is

$$f(r) = \frac{1}{2} \left[ \cos \left( \pi \frac{r - R_H}{\delta_T} \right) + 1 \right]. \quad (9)$$

This form was chosen in order to maintain analytic differentiability at the boundaries of the transition region. Although we have not studied the impact of using other weighting functions, it is safe to assume that (as long as the interpolation is consistent) any other form of  $f(r)$ , such as, e.g., a linear transition, would equally be possible.

(iii) To provide a full set of exchange partners for all magnetic moments with  $r < R_H + \delta_T$ , ghost magnetic moments are introduced in the transition region. The thickness of this shell is given by

$$\delta_G = \max\{|\mathbf{r}_i - \mathbf{r}_j|\} \quad \text{with} \quad J_{i,j} \neq 0, \quad (10)$$

where  $\mathbf{r}_i$  is the position of the magnetic moment  $i$ , which results eventually in the relation  $R_1 = R_H + \delta_T + \delta_G$ .

In the shell region, the atomistic core is surrounded by and attached to spherical shells of finite elements with radially increasing cell size. The starting point for the construction of these shells is an icosahedron that acts as a scaffolding structure, with geodesic domes [25] built around it, based on its triangular facets. We choose the initial construction frequency  $f_{\text{geo}}^{(1)}$  (the number of subdivisions of the spherical triangle edge) so that the edge length of subtriangles matches the edge length of tetrahedra in the core of the sphere. In each further shell  $n$ , we reduce the frequency to  $f_{\text{geo}}^{(n)} = f_{\text{geo}}^{(n-1)} - m$ , where  $m$  is a small integer that is typically between 2 and 4. Smaller values of  $m$  lead to a slower increase of cell size, a larger total sphere radius, and, consequently, more vertices. This increase of numerical costs results in smaller inhomogeneities of the mesh and, therefore, in a higher accuracy. The circumference radius  $r_{\text{geo}}^{(n)}$  of the scaffolding icosahedron for every additional shell  $n$  is chosen to be  $r_{\text{geo}}^{(n)} = r_{\text{geo}}^{(n-1)} + l_c^{(n)}$ , with  $l_c^{(n)}$  the average edge length of surface triangles in the new shell. Using this procedure, spherical shells are added until  $l_c^{(n)}$  is larger than the average edge length used for the sample mesh. Finally, the volume between the spherical surfaces is discretized into

tetrahedral simplex elements with a Delaunay algorithm using GMSH [26]. Since this triangulation is part of the preprocessing, the choice of parameters can be tuned carefully to ensure that the transition of cell sizes is smooth, thereby significantly improving the accuracy of the calculation of the exchange field and energy.

Figure 2 shows that the entire mesh is highly regular except for the transition between the core and the shell, which is an irregularity that cannot be avoided since it connects the atomistic core based on a Bravais lattice to the mesoscopic spherical shell.

At radii  $r > R_H + \delta_T$ , the simulations are purely micromagnetic. The radially increasing cell size of the shell region prevents an abrupt change of length scales, which could give rise to significant artifacts [24].

## B. Multiscale regions near the surface

Regions of interest traced by a MS can move to the surface of the sample, so that the MS may partially leave the sample volume. In that case, the MS must be cropped in order to preserve the shape and volume of the simulated sample, i.e., nodes of the MS outside the volume are discarded. If the protruding part of the MS is removed, the remaining internal nodes and elements of the MS generally do not form a set that can serve as a replacement for the sample surface without further corrections. To maintain the surfaces of the sample mesh, on one hand, and to avoid a time-consuming remeshing of the MS, on the other hand, a specific solution is needed, which in our case literally resembles a patch. If the MS is cropped, the gradual reduction of the discretization density is lost, resulting in a direct synchronization of nodes attached to very different cell size. To achieve a smooth transition, we use a set of typically 10 to 12 preprocessed micromagnetically treated calotte structures that connect the central parts of the sphere to the surface. A subset of typical calottes for a cylindrical structure is shown in Fig. 3. By using such ‘‘patches,’’ we abandon the generality of the code, since the shape of each calotte is prepared to fit to the sample surface: in this case, that of a cylinder. While it is straightforward to generalize this approach to other geometries, the preparation of the meshes must be performed for each specific geometry. The calottes used in our case penetrate the sample by a thickness of twice the discretization size of the background mesh. The set of calottes is designed so that the change of discretization density is compatible to the MS at a given distance from the surface: If the MS barely touches the surface, there is no particular need for adjustments, but as the core of the MS approaches the surface, the calotte structure must be replaced by one that covers a large difference in discretization density.

## C. Hierarchical coupling of the discretization grids

So far, if we neglect the connecting boundary shells discussed before, we have four distinct discretization levels that enter into the simulation:

- (i) the atomistic Heisenberg structure in the core of the MS,
- (ii) the micromagnetic outer part of the MS with radially increasing cell size,

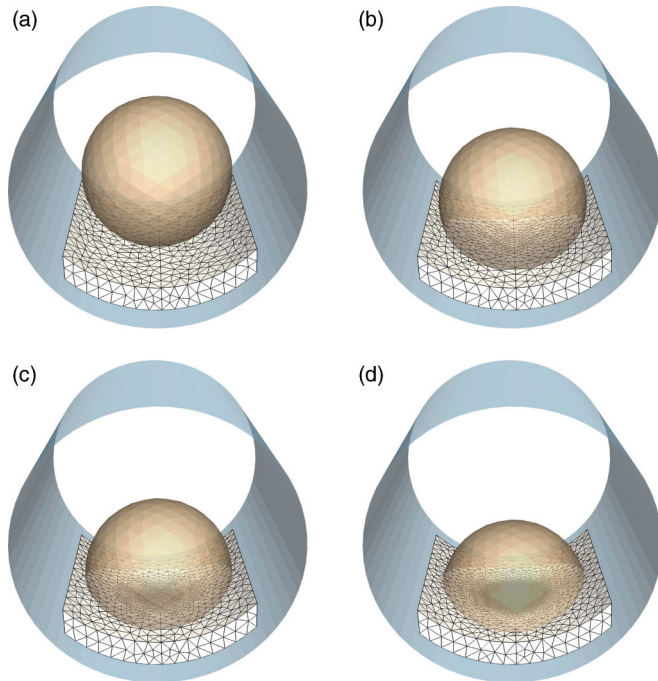


FIG. 3. (Color) Set of calotte structures acting as “refinement patches” for different distances of the MS to the boundary of the cylindrical sample. As the MS reaches the surface, the transition is achieved with calotte meshes of appropriate discretization density, which are chosen dynamically from a predefined set of meshes according to the penetration depth of the MS into the surface.

(iii) the “patches” in the form of calotte structures with spatially varying discretization density, and

(iv) the original mesh of the sample, which represents the background into which all of the entities listed above are embedded.

Each of these discretized regions is connected to a set of data for the magnetic structure, and they can partly or entirely share fractions of the volume of the sample. In order to obtain a consistent representation, a hierarchical structure is defined according to the list shown above, so that the smallest available discretization cell is decisive and donates its magnetic properties to those structures with larger cell size. This means that the magnetic moments of the Heisenberg model are used to determine the magnetization direction at nodes of calotte structure located in the Heisenberg region, that the finer discretization in the calotte structure dictates the magnetization direction of the background mesh, etc. This is a simplified and general description in the sense that there is, of course, also, e.g., a coupling of the background onto the MS, but the hierarchical order is, in principle, as listed above.

To couple the MS to the background, i.e., to the ferromagnetic volume into which the Bloch point is embedded, each surface node of the MS receives the magnetic orientation and the effective field components by interpolation from the nodes of the tetrahedron of the static background mesh containing it. Conversely, a handshake between the regions is obtained as the data of each background node located inside the MS is assigned by the MS sphere, except for those background nodes which assign data to the boundary nodes of the MS

themselves. In general, a transition region between the two meshes (outer MS sphere and background) could be included, similar to the one used to connect the Heisenberg region with the micromagnetic inside the MS. In Sec. VI, it is shown that better results are obtained without such an additional transition region.

Note that the magnetostatic field contribution represents an exception of the coupling discussed above. As analytic calculations have shown, the magnetostatic energy density in the vicinity of a Bloch point is significantly smaller than the exchange energy [7,8,27]. On a local scale, the dipolar energy (and the resulting effective field) near a Bloch point is merely a perturbation that—unlike the exchange term—does not require any particular correction. It can safely be calculated using the background mesh only. The result is then interpolated onto the vertex positions of the MS/“patch” meshes in order to account for the contribution of the dipolar field to the effective field.

#### D. Intersections of multiscale spheres

During a simulation, inhomogeneities may be distributed in space such that several multiscale regions and calotte structures are required simultaneously. The code can handle such situation, but some attention is necessary when different MS and/or calotte structures intersect. In order to synchronize the various regions, we use a hierarchical approach to decide which mesh is chosen as the source of the magnetic properties (the donor) and which one is adapted to them (the acceptor). Several cases can be encountered:

(i) If two MS are nearly concentric, the atomistic region of each sphere is overlapping but it is basically identical. There is no reason to favor one MS over the other in that purely atomistic region and there is no requirement to interpolate or to change anything.

(ii) When the atomistic region of one MS enters the continuum region of another MS, the values of the Heisenberg region are prioritized. The Heisenberg structure imprints the magnetization at any node of the finite-element mesh in that region.

(iii) When two or more finite element regions of multiscale spheres overlap, the values at the nodes of the elements in one sphere may be adapted according to the values of the other sphere. For this, the role of the donor is first ascribed to the MS for which a given node is closest to the center point. This is, however, only a necessary, and not a sufficient, condition to discard the original values. To decide whether the values of the donor MS are used to interpolate onto the acceptor MS, we introduce a further criterion, which is based on the position of the nodes of the tetrahedral element of the donor sphere containing the acceptor node. We first determine the distance between these nodes and the center of the donor sphere and take the largest value. If this value is smaller than the distance between the acceptor node and the center of the acceptor sphere, the interpolation is performed, else the value remains unchanged, thereby preventing repeated interpolations that could introduce artifacts in the magnetic structure [28].

(iv) If a calotte structure is used, the magnetization is interpolated from the elements of the calotte acting as a donor onto the background mesh. If both the donor and the acceptor mesh are calotte structures, an interpolation is performed only

if the cell size of the donor cell is smaller than the smallest cell size in the Voronoi cell belonging to the acceptor node.

In the code, more details are considered in terms of donor and acceptor mesh, but most of these conventions are uncritical and the procedure described above should be sufficient to obtain a general picture of the complications arising and the procedures applied in the handshake regions of different meshes.

### E. Dynamics

The dynamics of the magnetization within the multiscale model is governed by the Landau-Lifshitz-Gilbert equation. The equation is applied to calculate the orientation of the magnetic moments in the Heisenberg model and the direction of the magnetization in the micromagnetic region—both denoted here as  $\mathbf{m}$ ,

$$\frac{d\mathbf{m}}{dt} = -\gamma\mathbf{m} \times \mathbf{H}_{\text{eff}} + \alpha \left[ \mathbf{m} \times \frac{d\mathbf{m}}{dt} \right], \quad (11)$$

where  $\gamma$  is the gyromagnetic ratio and  $\alpha$  is the phenomenological Gilbert damping parameter. The effective field  $\mathbf{H}_{\text{eff}}$  is defined as

$$\mathbf{H}_{\text{eff}}^{\text{MM}} = -\frac{\delta e_{\text{tot}}}{\mu_0 M_s \delta \mathbf{m}}, \quad (12)$$

$$\mathbf{H}_{\text{eff}(i)}^{\text{Hei}} = -\frac{V_i \delta e_{\text{tot}}}{\mu_0 \mu_i \delta \mathbf{m}}, \quad (13)$$

where  $\mu_0$  is the vacuum permeability,  $e_{\text{tot}}$  is the total free-energy density,  $M_s$  is the saturation magnetization,  $\mu_i$  is the magnetic moment with index  $i$ , and  $V_i$  is its associated volume.

By creating a joint array of magnetic orientations combining the arrays of the involved meshes, we use Sundials' CVODE solver [29] in the same way as in the original, purely micromagnetic GPU-accelerated version of TETRAMAG [23].

We dynamically track the region of interest, e.g., a Bloch point or (as discussed in the following test case) a vortex, and move the sphere if the region of interest is off-centered by a small number of lattice constants, usually one or two. The tracking of a Bloch point is a three-step process in order to save computational time. First, all cells of all MSs as well as the background mesh are tested for a change of sign of the  $m_x$ ,  $m_y$ , and  $m_z$  component, which is a necessary condition for the presence of a Bloch point inside of a cell. Second, for all those cells  $n$  fulfilling this condition, we solve the system of linear equation

$$\sum_{i=1}^4 f_i^{(n)}(\mathbf{r}_{\text{BP}}) \mathbf{m}_i^{(n)} = 0, \quad (14)$$

where  $\mathbf{r}_{\text{BP}}$  is the position of the Bloch point,  $f_i^{(n)}(\mathbf{r})$  are the shape function of tetrahedral finite elements  $n$ , and the index  $i$  is the local number of the element's vertex. If  $\mathbf{r}_{\text{BP}}$  is inside of the circumsphere of the tetrahedron  $n$ , we identify  $\mathbf{r}_{\text{BP}}$  as the Bloch-point position which is located within the cell  $n$ . For the case in which the Bloch point is in an adjacent finite element, we choose the element for which the Bloch point is closest to the in-sphere center of the tetrahedron. Usually, the Bloch point can be found in the background mesh as well as in at least one MS. Therefore, in a last step, we compare the lists

of Bloch-point coordinates obtained from different meshes and compare these positions with each. More specifically, we ensure that the same Bloch point has been detected in the different meshes, and we do this by comparing the variations of the Bloch-point positions with the cell size of the meshes. Finally, once this is confirmed, we retain only the Bloch-point position that is calculated using the smallest tetrahedron.

Every propagation step moves the structure by an integer number of lattice vectors. This ensures that interpolations are performed only in the micromagnetic part, but not in the Heisenberg region of the MS. The position of the atoms remains fixed.

### VI. TEST OF THE CODE

Before studying the structure and the propagation of Bloch points with this complex algorithm, it is necessary to gain confidence into its capabilities and to test its reliability. Most importantly, it is necessary to ensure that the complicated nesting of meshes does not introduce numerical artifacts, such as artificial oscillations, instabilities, or increased damping. In order to investigate such effects, or the absence thereof, we study the gyrotropic motion of a vortex in a thin-film element. Such situations of gyrating vortices in patterned magnetic elements have been studied intensively over the past years and the physics is well understood (cf., e.g., Ref. [31] and references therein). This example can be considered as a typical problem that modern micromagnetic simulation codes such as TETRAMAG can simulate with high accuracy, yet it is sufficiently nontrivial to unveil possible problems connected with the dynamic multiscale-multimodel code.

This case does not contain a singularity, hence an atomistic treatment is unnecessary. Nevertheless, we introduce a MS here which resolves the core of the vortex with atomistic accuracy. The position of the vortex core can be traced conveniently by using the intersection of the isosurfaces  $m_x = 0$  and  $m_y = 0$  of the in-plane magnetization components (cf. Ref. [30]). Since these isosurfaces can be tilted, so that their crossing line is not necessarily parallel to the  $z$  axis, we chose the intersection in the middle,  $z = t/2$ , of the disk to determine the vortex position, where  $t$  is the thickness and the bottom surface is at  $z = 0$ .

The material parameters of the simulations are the typical values of permalloy, with exchange stiffness  $A = 1.31 \times 10^{-11}$  J/meter, saturation magnetization  $\mu_0 M_s = 1.00$  T, and negligible magnetocrystalline anisotropy. The damping is set to  $\alpha = 0.02$ . The exchange length  $l_{\text{exc}}$  of this material is about 5.7 nm, from which the vortex core radius can be estimated to [32]

$$r_{\text{core}} = 0.68 l_{\text{exc}} \left( \frac{h}{l_{\text{exc}}} \right)^{1/3} \approx 6.1 \text{ nm}. \quad (15)$$

In the vortex core, the magnetization rotates by  $180^\circ$ , which according to Eq. (7) corresponds to  $\lambda \approx 12.2$  nm. For the Heisenberg parameters, we use a bcc lattice with lattice constant  $a = 2.86$  Å, resulting in  $\delta_G \approx 2.2$  Å. This yields a magnetic moment of  $\mu = 1.01 \mu_B$  per lattice site. The Heisenberg exchange constant between nearest neighbors is  $J = 11.79$  meV. By virtue of Eq. (7), we choose  $R_1 = 7$  nm with  $\delta_T = 2$  nm in order to keep the local micromagnetic error below 0.1% for a

180° rotation within the diameter of the core region. The disk is meshed with a tetrahedral cell size of 1.75 nm.

As shown in Fig. 4, the dynamic multiscale-multimodel algorithm perfectly reproduces the results obtained by the micromagnetic code. The MS sphere follows the position of the vortex core, as can be seen in a movie provided in the Supplemental Material [33]. This agreement is reassuring because it demonstrates that in spite of the numerous interpolations, the simultaneous use of different models, and the enormously different length scales that are bridged at any time step of the calculation, the result remains unchanged. In the two frames shown on the upper part of Fig. 4, the evolution of the energy and the average magnetization component  $\langle m_y \rangle$  are displayed as a function of time. In both cases, the data obtained from the multimodel code perfectly matches the data of the micromagnetic code, so that the lines cannot be distinguished on that scale. In order to examine minor variations, we examined this data in greater detail. More

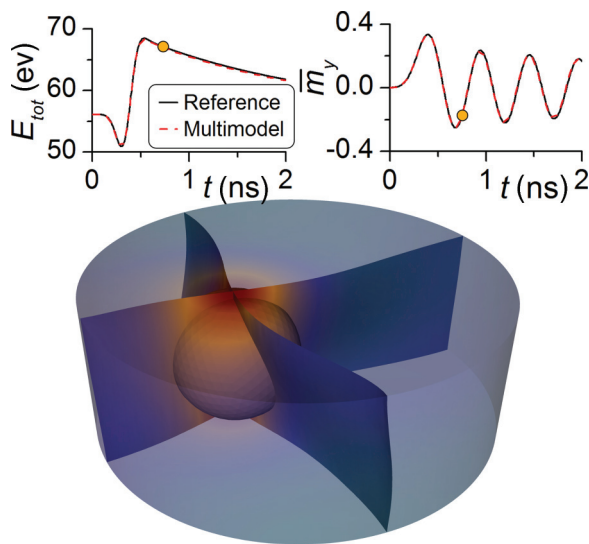


FIG. 4. (Color) As a test case for the multimodel-multiscale code, we use a permalloy disk of 100 nm diameter and 35 nm height with a vortex structure. A spatially homogeneous in-plane field pulse with Gaussian time profile is applied to the relaxed vortex structure. The field pulse is applied along the  $x$  axis; it has an amplitude of 50 mT, width  $\sigma = 100$  ps, and a peak delay of  $t_{Max} = 300$  ps. This perturbation of the system generates a well-known micromagnetic low-frequency excitation (gyrotropic motion) which represents a spiraling motion of the vortex core around the equilibrium position. The background mesh has a cell size of 1.75 nm. On the upper left, the evolution of the total energy of the system is displayed as a function of time, while on the upper right, the spatially averaged and normalized  $y$  component of the magnetization  $\langle m_y \rangle$  is shown. The results obtained from the purely micromagnetic code and the multiscale-multimodel code are identical. The main frame on the bottom shows a snapshot of the magnetic structure at the moment indicated by the yellow dots in the upper frames. The color code represents the out-of-plane component  $m_z$  of the magnetization and the semitransparent representation shows the position of the MS sphere at the core of the vortex. In the core of that sphere, the magnetic structure is calculated on an atomistic level. The crossing ribbons are the  $m_x = 0$  and  $m_y = 0$  isosurfaces, which we use routinely to track the position of the vortex (cf. Ref. [30]).

specifically, we used this data to investigate the necessity of an internal transition region between the MS sphere and the background. Such a transition region was previously introduced to connect the micromagnetic model with the Heisenberg calculation. In that case, the accuracy of the calculation increased with the width of the transition region. Remarkably, this is not true for the connection of the outer part of the MS sphere to the background. There, a direct connection of the nodes on the outer shell of the MS to the background gives the best results. This is shown in Fig. 5, where the previously described test case of a gyrating vortex is simulated with identical conditions but different thickness  $\delta_T$  of a transition region at the boundary of the MS. This transition region is illustrated in Fig. 2 as the shading where the color changes from orange to green. While in all cases the deviations from the micromagnetic reference result are very small, the results clearly show that such a transition is detrimental to the accuracy. A direct connection of the nodes at the boundary of the MS sphere to the background leads to better agreement than a weighted averaging of the contributions from the outer regions of the MS and the background. The accuracy of the simulation is considerably lower when  $\delta_T$  exceeds about one nanometer. The results indicate that for the given discretization, it is best to discard any transition region

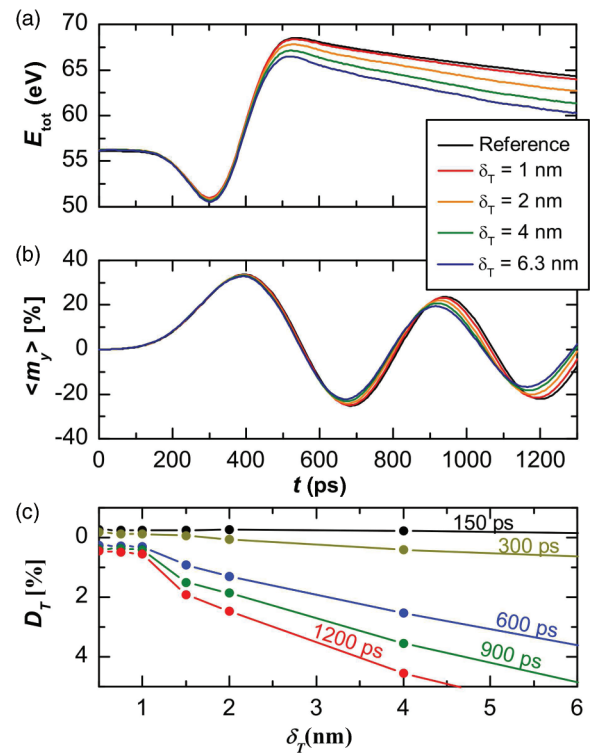


FIG. 5. (Color) (a) Total energy and (b) average  $y$  component of the magnetization  $\langle m_y \rangle$  for the previously discussed case of a gyrating vortex. The various lines correspond to the results obtained with transition regions of different thickness  $\delta_T$ . (c) The error of the total energy connected with the multiscale-multimodel method as a function the thickness of the transition region  $\delta_T$ . Each of the lines refers to a moment in time (as indicated) after the beginning of the simulation at  $t = 0$ . Here, the exact value of the energy is assumed to be the one obtained from the micromagnetic simulation, and the deviation from this value is displayed in percentage points.

between the two meshes and use the coupling rules described in Sec. V C instead.

In addition to the simulations with nearest-neighbor exchange interaction, we studied the same systems with the Heisenberg exchange parameters of Fe, as described by Pajda *et al.* [34], with a total of 144 neighbors, scaled to match the micromagnetic exchange stiffness  $A = 1.31 \times 10^{-11}$  J/m of permalloy. This yielded no significant change of the results compared to those obtained with a nearest-neighbor exchange interaction.

## VII. BLOCH-POINT MOTION IN A SOFT-MAGNETIC CYLINDER

As mentioned in Sec. I, an important example for the propagation of Bloch points is the magnetization reversal of a sufficiently large soft-magnetic cylinder [5]. In soft-magnetic nanowires, the magnetization aligns almost everywhere with the wire axis because of the predominant impact of shape anisotropy, and the regions separating domains with opposite magnetization are head-to-head or tail-to-tail domain walls. Although countless studies have been reported over the past decade investigating these domain walls, they were almost exclusively limited to the simple case of flat strips with a rectangular cross section, where head-to-head structures are either transverse or vortex walls, depending on the width and thickness [36]. In cylindrical wires with circular cross sections, the situation is different. There, the magnetic structure has the possibility to preserve the axial symmetry, resulting in a Bloch point in the middle of an axial vortex wall. In spite of its high energy density, a Bloch-point structure becomes energetically favorable at sufficiently large wire radius, owing to the cumulative long-range magnetostatic interaction which outweighs the effect of the strong but short-range exchange interaction. From a magnetostatic perspective, the Bloch point is the most convenient arrangement of a head-to-head domain wall in a cylinder: The magnetization aligns everywhere with the surface, thereby preventing surface charges [37]. Moreover, the axial vortex is a divergence-free arrangement, which prevents magnetostatic volume charges [37]. This nearly perfect suppression of magnetostatic fields is the reason for the formation of Bloch points in thick cylinders. It is well known that Bloch points carry a magnetostatic monopole charge [38]. Therefore, this type of domain wall is also not completely free of stray fields. However, the magnetostatic monopole contribution is inevitable in any kind of head-to-head domain wall [39] and the Bloch point therefore represents the smallest possible source of magnetostatic fields for the given boundary conditions. The only energy term that tends to suppress the formation of the Bloch point is the exchange interaction. But the role of the exchange interaction becomes negligible if the sample size is sufficiently large—so large that minimizing the magnetostatic energy is the predominant tendency. Precise boundaries describing the transition region between transverse domain walls and vortex domain walls with a Bloch point have not yet been determined. Typical values for the minimum diameter of a soft-magnetic cylinder with a Bloch point seem to be above 40 nm [39,40], since simulations indicate that at larger wire diameters the one-dimensional, transverse domain-wall type becomes unstable.

When the vortex domain walls in the cylinder move, e.g., because an external magnetic field is applied, the Bloch point can propagate along the cylinder axis. Earlier publications [5,13,41] studied this type of reversal process in the framework of pure micromagnetism, even though a rigorous treatment of the Bloch-point structure and its dynamics requires a multi-model method. Using our multiscale algorithm, we examined the propagation of a Bloch point in a 4- $\mu$ m-long cylinder with a diameter of 60 nm, with material/simulation parameters according to Ref. [35]. We distinguished two cases: one in which the cylinder axis points in the (100) direction and another in which it points along the (110) direction of the lattice. On a single NVIDIA GTX 580 GPU, the simulations presented here require, on average, a time ratio of 1.4 ps per minute.

The chirality of the domain wall, defined as the sense of circulation of the magnetization in the vortex wall combined with the direction of the external field, determines the degree of stability of the domain wall during its motion. This is analogous to the dynamics of vortex domain walls in nanotubes [42,43], where the highest stability is obtained for head-to-head domain walls with right-handed chirality and tail-to-tail domain walls with left-handed chirality, respectively. If we discard the unstable combinations, it is sufficient to analyze only the right-handed chirality of the head-to-head type, since it is identical to the other combination due to time-inversion symmetry.

In the equilibrium (zero-field) configuration, the Bloch point resides in the center of the vortex domain wall and the magnetic configuration displays cylindrical symmetry. Close to the Bloch point, we find inflow angles  $\gamma$  of  $72.3^\circ$  and  $73.1^\circ$  for the cases of the (110) and the (100) orientation of the lattice, respectively. Those values lie within the interval predicted by Döring [8] ( $\gamma = 67.6^\circ$ ) and by Pylypovsky *et al.* [27] ( $\gamma = 75.1^\circ$ ).

Below  $H = 1$  and  $H = 1.8$  mT in the cases of (110) and (100) orientation of the cylinder axis, respectively, the Bloch point experiences a pinning. This effect was theoretically predicted by Reinhardt [44] in 1973, and it is clearly visible in Fig. 6. The last point in Fig. 6 at which the velocity is zero corresponds to the depinning field, which was determined by an adiabatic increase of the external field with a rate of 2 mT/ns. If the applied field is sufficiently large to overcome this lattice-orientation-dependent pinning, the Bloch point and the domain wall propagate smoothly in the axial ( $z$ ) direction. During an initial acceleration period, the system preserves the cylinder symmetry and the combination of Bloch point and domain wall reaches a field-dependent maximum speed. This velocity is plotted with filled symbols in Fig. 6 and connected by solid lines. Figure 7 shows the evolution of the Bloch-point velocity as a function of the external field, with the cylinder axis oriented in the (100) direction. Our results indicate a significant influence of the lattice orientation with respect to the cylinder axis on the domain-wall dynamics. First, the depinning field is much lower in the (100) case compared to the (110) case. Second, we obtain a markedly reduced domain-wall velocity at the same external field for the case of the (110) axis orientation compared to the (100) axis orientation. In both cases, the magnetic structure of the domain wall moving at maximum velocity displays a metastable configuration, whose stability improves with increasing external field. But after a

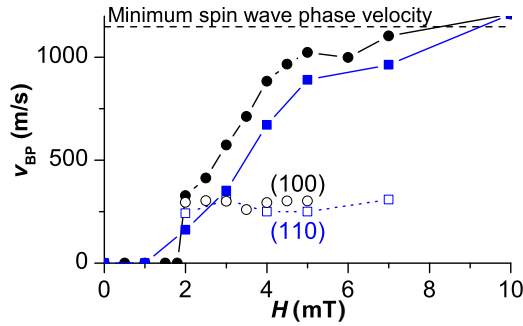


FIG. 6. (Color online) Bloch-point velocity as a function of the applied field in a wire with a diameter of 60 nm. Different propagation behaviors are found, depending on the relative orientation of the cylinder axis and the atomic lattice. The last data point with zero velocity represents the depinning field. For both orientations, two metastable dynamic domain-wall configurations can be distinguished. The first is a propagation mode with almost field-independent velocity, as indicated by empty symbols. The system can also display a second propagation mode, with a different domain-wall configuration and for which the velocity increases significantly with the external field.

certain, field-dependent period, the domain wall undergoes a structural transition and the velocity drops to a constant value of  $v \approx 300$  m/s—for both relative orientations of the lattice and the cylinder axis, as marked by open symbols and connected by dotted lines in Fig. 6. Note that the Bloch point is still in the middle of the domain wall. The difference is that the magnetic structure around the Bloch point is distorted, leading to an unforeseen spontaneous break of symmetry. The different domain-wall structures are shown in Fig. 8, where two snapshots of the Bloch-point propagation are displayed: one for the initial configuration and one after the conversion into a tilted domain-wall structure. In this case, an axial field of  $H_{\text{ext}} = 2$  mT is applied and the cylinder axis is along the (100) orientation. These two effects, i.e., the metastable dynamic domain-wall profile and the impact of the lattice orientation on the dynamics of the Bloch point and the domain wall containing it, are most pronounced for domain-wall speeds below

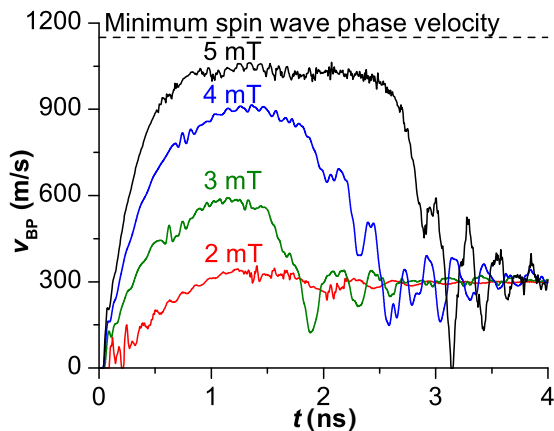


FIG. 7. (Color online) Evolution of the Bloch-point velocity vs times in the low field (regime below the magnonic limit) for a wire with a diameter of 60 nm and a cylinder axis oriented in the (100) direction.

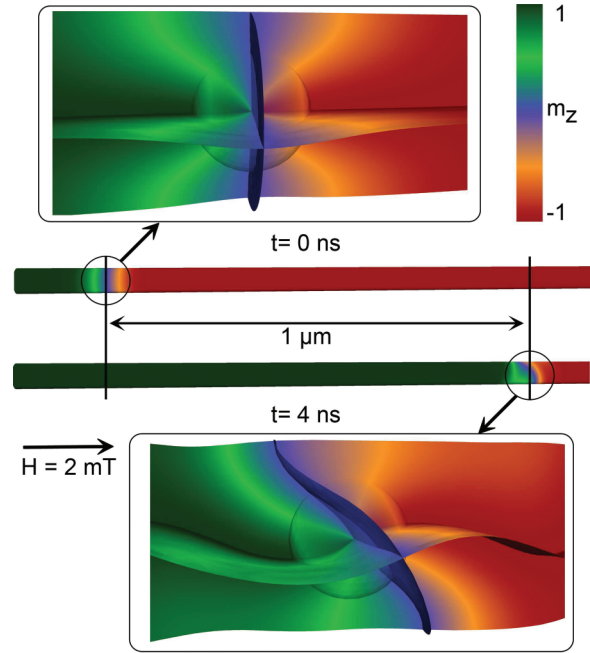


FIG. 8. (Color) Snapshots of the simulated vortex domain-wall (DW) propagation in a ferromagnetic cylinder [35] with a Bloch point in its core. The two magnified images show the magnetic configuration around the Bloch point in the equilibrium configuration and after applying an external field of 2 mT for four nanoseconds. The crossing of the three  $m_{\{x,y,z\}} = 0$  isosurfaces indicates the position of the BP in the center of the multimodel sphere, and the coloring represents the axial magnetization component.

the minimum spin-wave phase velocity. At velocities above the “magnonic limit” [45,46], the transition to another type of domain-wall propagation is observed, with completely different features, which will be the subject of a forthcoming paper.

As the driving field increases, the differences resulting from different lattice orientations diminish. From this, it can be concluded that an atomistic/multimodel treatment may not be necessary if two conditions are fulfilled: The mesh size should correspond to the atomistic lattice parameter and the driving field should be strong enough to overcome any pinning effect. Nevertheless, it may be preferable to use the multimodel algorithm, not the least because in the case of nearest-neighbor interaction, the numerical costs connected with a Heisenberg model are smaller than those of a finite-element calculation with cell size in the range of the atomic lattice parameter. This is because a typical Voronoi cell includes 10 to 20 vertices, whereas a nearest-neighbor interaction takes into account only six to eight neighbors.

### VIII. SUMMARY

We have presented in detail the implementation of a dynamic multiscale-multimodel algorithm which combines a micromagnetic finite-element code with a classical Heisenberg model. The code runs entirely on graphic cards, which allows for a fast computation of the complex interacting meshes involved in the simulation. An analytical estimation has been derived to calculate the critical distance between misaligned magnetic moments below which an atomistic

treatment becomes decisive. This critical size is used as a criterion for the minimum diameter of the region in the model in which exchange interaction is treated purely by the Heisenberg model. We have shown that the numerically critical part of the method, i.e., the interface between the sample and the implanted multiscale sphere, gives rise to a local error of less than one percent, which is good enough to use the method for reliable future studies on the dynamics of Bloch points. The code has been thoroughly tested, ensuring that the simultaneous treatment of different methods does not introduce artifacts. The multiscale region consists of a preprocessed sphere that can move through the sample without the need of numerically expensive remeshing processes. Owing to this ability to trace regions of interest dynamically, we could demonstrate in an example study the dynamics of Bloch points with unprecedented accuracy.

We showed that the dynamics of vortex domain walls in cylindrical nanowires containing a Bloch point depends on the orientation of the lattice with respect to the cylinder axis for a broad range of external fields. For that system, we confirmed the existence of a finite depinning field, as well as two metastable propagation modes—one with a constant propagation velocity for a broad range of external fields and one with an almost constant mobility for external fields above the depinning field.

The dynamics of Bloch points can be expected to contain a number of surprising effects, similar to the rich variety of effects that have been discovered concerning the dynamics of vortices and domain walls. The algorithm presented in this paper enables a precise study of the Bloch-point dynamics for different lattice types and orientation. More studies on this topic will be published soon.

- 
- [1] A. Aharoni, *Introduction to the Theory of Ferromagnetism*, 2nd ed. (Oxford University Press, Oxford, UK, 2000).
- [2] W. F. Brown, *Micromagnetics* (Interscience, New York, 1963).
- [3] H. Kronmüller, in *Handbook of Magnetism and Advanced Magnetic Materials*, edited by H. Kronmüller and S. S. P. Parkin (Wiley, New York, 2007).
- [4] E. H. Frei, S. Shtrikman, and D. Treves, *Phys. Rev.* **106**, 446 (1957).
- [5] A. Arrott, B. Heinrich, and A. Aharoni, *IEEE Trans. Magn.* **15**, 1228 (1979).
- [6] A. Hubert and W. Rave, *J. Magn. Magn. Mater.* **184**, 67 (1998).
- [7] E. Feldtkeller, *Zeitsch. Angew. Phys.* **19**, 530 (1965).
- [8] W. Döring, *J. Appl. Phys.* **39**, 1006 (1968).
- [9] L. Landau and E. Lifshitz, *Phys. Zeitsch. der Sow.* **8**, 153 (1935).
- [10] T. Gilbert, *Phys. Rev.* **100**, 1243 (1955).
- [11] T. Gilbert, *IEEE Trans. Magn.* **40**, 3443 (2004).
- [12] O. C. Zienkiewicz, R. L. Taylor, and J. Z. Zhu, *The Finite Element Method at Its Basis and Fundamentals*, 6th ed. (Elsevier, New York, 2005).
- [13] A. Thiaville, J. M. García, R. Ditttrich, J. Miltat, and T. Schrefl, *Phys. Rev. B* **67**, 094410 (2003).
- [14] S. Gliga, Y. Liu, and R. Hertel, *J. Phys.: Conf. Ser.* **303**, 012005 (2011).
- [15] F. García-Sánchez, O. Chubykalo-Fesenko, O. Mryasov, and R. W. Chantrell, *Physica B: Condens. Matter* **372**, 328 (2006).
- [16] W. Heisenberg, *Z. Phys.* **33**, 879 (1925).
- [17] A. Hubert and R. Schäfer, *Magnetic Domains: The Analysis of Magnetic Microstructures*, 1st ed. (Springer, Berlin, 1998).
- [18] K. M. Lebecki, D. Hinzke, U. Nowak, and O. Chubykalo-Fesenko, *Phys. Rev. B* **86**, 094409 (2012).
- [19] E. Galkina, B. Ivanov, and V. Stephanovich, *J. Magn. Magn. Mater.* **118**, 373 (1993).
- [20] R. G. Elías and A. Verga, *Eur. Phys. J. B* **82**, 159 (2011).
- [21] T. Jourdan, A. Marty, and F. Lançon, *Phys. Rev. B* **77**, 224428 (2008).
- [22] G. Hrkac, T. G. Woodcock, C. Freeman, A. Goncharov, J. Dean, T. Schrefl, and O. Gutfleisch, *Appl. Phys. Lett.* **97**, 232511 (2010).
- [23] A. Kákay, E. Westphal, and R. Hertel, *IEEE Trans. Magn.* **46**, 2303 (2010).
- [24] R. E. Miller and E. B. Tadmor, *Model. Simulat. Mater. Sci. Eng.* **17**, 053001 (2009).
- [25] R. B. Fuller, *Building Construction* (US 2682235, 1954).
- [26] C. Geuzaine and J.-F. Remacle, *Int. J. Numer. Methods. Eng.* **79**, 1309 (2009).
- [27] O. V. Pylypovskiy, D. D. Sheka, and Y. Gaididei, *Phys. Rev. B* **85**, 224401 (2012).
- [28] R. Hertel and H. Kronmüller, *IEEE Trans. Magn.* **34**, 3922 (1998).
- [29] A. C. Hindmarsh, P. N. Brown, K. E. Grant, S. L. Lee, R. Serban, D. E. Shumaker, and C. S. Woodward, *ACM Trans. Math. Software* **31**, 363 (2005).
- [30] R. Hertel and C. M. Schneider, *Phys. Rev. Lett.* **97**, 177202 (2006).
- [31] S.-B. Choe, Y. Acremann, A. Scholl, A. Bauer, A. Doran, J. Stöhr, and H. A. Padmore, *Science* **304**, 420 (2004).
- [32] N. Usov and S. Peschany, *J. Magn. Magn. Mater.* **118**, L290 (1993).
- [33] See Supplemental Material at <http://link.aps.org/supplemental/10.1103/PhysRevB.89.134403> for a movie showing that the MS sphere follows the position of the vortex core.
- [34] M. Pajda, J. Kudrnovský, I. Turek, V. Drchal, and P. Bruno, *Phys. Rev. B* **64**, 174402 (2001).
- [35] The material of the 4- $\mu\text{m}$ -long cylinder with 60 nm diameter is a bcc crystal with lattice constant  $a = 2.866 \text{ \AA}$ , and a magnetic moment of one Bohr magneton per lattice site. The atomistic model considers nearest-neighbor interaction with an exchange constant of  $J = 11.79 \text{ meV}$ . In micromagnetic terms, these parameters correspond to a saturation magnetization of  $\mu_0 M_s = 1.00 \text{ T}$  and an exchange stiffness of  $A = 1.31 \times 10^{-11} \text{ J/m}$ . The sample (background) mesh consists of tetrahedrons with 3 nm cell size, resulting in 494 914 vertices. The multimodel sphere has a total diameter of 37 nm, and an atomistic core region with a diameter of 14 nm, including a model transition region of 2 nm width.
- [36] R. McMichael and M. Donahue, *IEEE Trans. Magn.* **33**, 4167 (1997).
- [37] W. F. Brown, *Magnetostatic Principles in Ferromagnetism* (North-Holland, Amsterdam, 1962).

- [38] A. P. Malozemoff and J. C. Slonczewski, *Magnetic Domain Walls in Bubble Materials* (Academic, New York, 1979).
- [39] R. Hertel and A. Kákay, [arXiv:1401.0909](https://arxiv.org/abs/1401.0909).
- [40] R. Hertel and J. Kirschner, *Phys. B: Condens. Matter* **343**, 206 (2004).
- [41] R. Hertel and J. Kirschner, *J. Magn. Magn. Mater.* **278**, L291 (2004).
- [42] P. Landeros and A. S. Núñez, *J. Appl. Phys.* **108**, 033917 (2010).
- [43] M. Yan, C. Andreas, A. Kákay, F. García-Sánchez, and R. Hertel, *Appl. Phys. Lett.* **100**, 252401 (2012).
- [44] J. Reinhardt, *Int. J. Magn.* **5**, 263 (1973).
- [45] M. Yan, C. Andreas, A. Kákay, F. García-Sánchez, and R. Hertel, *Appl. Phys. Lett.* **99**, 122505 (2011).
- [46] M. Yan, A. Kákay, C. Andreas, and R. Hertel, *Phys. Rev. B* **88**, 220412(R) (2013).